Effective temperature dynamics of shear bands in metallic glasses

Eric G. Daub, David Klaumünzer, and Jörg F. Löffler

Phys. Rev. E **90**, 062405 — Published 19 December 2014

DOI: 10.1103/PhysRevE.90.062405

Effective temperature dynamics of shear bands in metallic glasses

Eric G. Daub,[1,2,3] David Klaumünzer,[2] and Jörg F. Löffler[2]

[1]*Geophysics Group and Center for Nonlinear Studies,*
Los Alamos National Laboratory, Los Alamos, NM, 87545, USA
[2]*Laboratory of Metal Physics and Technology,*
Department of Materials, ETH Zurich, 8093 Zurich, Switzerland
[3]*Center for Earthquake Research and Information,*
University of Memphis, Memphis, TN, 38152, USA

Abstract

We study the plastic deformation of bulk metallic glasses with Shear Transformation Zone (STZ) Theory, a physical model for plasticity in amorphous systems, and compare it with experimental data. In STZ Theory, plastic deformation occurs when localized regions rearrange due to applied stress and the density of these regions is determined by a dynamically-evolving effective disorder temperature. We compare the predictions of STZ Theory to experiments that explore the low-temperature deformation of Zr-based bulk metallic glasses via shear bands at various thermal temperatures and strain rates. By following the evolution of effective temperature with time, strain rate, and temperature through a series of approximate and numerical solutions to the STZ equations, we successfully model a suite of experimentally observed phenomena, including shear-band aging as apparent from slide-hold-slide tests, a temperature-dependent steady-state flow stress, and a strain rate- and temperature-dependent transition from stick-slip (serrated flow) to steady-sliding (non-serrated flow). We find that STZ theory quantitatively matches the observed experimental data and provides a framework for relating the experimentally measured energy scales to different types of atomic rearrangements.

I. INTRODUCTION

Deformation and flow in amorphous materials, such as glasses, foams, colloids, thin films, and granular materials, are not completely understood, and scientists do not have a first principles physics-based model for how amorphous materials deform and fail. The dynamics of deformation exhibit a wide range of phenomena, including plastic deformation once the yield stress is exceeded, strain and strain rate dependence of the flow stress, localization of strain, and stick-slip behavior [1–4]. Because amorphous materials exhibit similar types of macroscopic behavior and all are characterized by a disordered microscopic structure, development of a physical theory for deformation and failure that provides predictive power has been a subject of considerable research.

An example of such an amorphous material is a bulk metallic glass. Bulk metallic glasses, which are formed by rapidly cooling a melt of a particular composition, are of potential interest in numerous material applications, as their amorphous atomic structure leads to a lack of dislocations which carry the plastic deformation in crystalline metals [5–7]. Therefore, metallic glasses deform elastically up to large strains and stresses [8–11]. However, when bulk metallic glasses do deform plastically, they often fail catastrophically due to the formation of localized shear bands [12–15]. Understanding the basic physics of bulk metallic glass plasticity remains an important research problem for exploring the basic physics of glasses, for developing applications utilizing these materials, and for predicting the dynamics of deformation and failure of amorphous materials in general.

Theoretical studies of the deformation and flow of amorphous materials typically fall into two categories. At the microscopic scale, molecular dynamics studies probe disordered, glassy materials at the atomic scale [16, 17], providing microscopic resolution of atomic displacements and rearrangements. These studies have been invaluable in attempting to understand the atomic scale mechanisms responsible for deformation, but can only be conducted over limited length and time scales, scales much smaller than those typically probed by experiments. At the other extreme, phenomenological constitutive models, based primarily on experimental data, have been developed to describe material deformation and failure. This approach has been an extensive part of studies of granular fault materials in the context of earthquakes through the phenomenological Dieterich-Ruina friction laws [18, 19]. Constitutive models can capture some of the dynamics observed on the length and time scales of experiments, but provide limited physical insight into the deformation process.

Attempts to bridge these two approaches has been the goal of many theoretical models in recent years, where one attempts to gain insight from microscopic mechanisms determined in atomistic simulations, while producing a continuum model that can be applied at scales similar to those of experiments. Some approaches start from an inherently liquid-like model [20, 21], to which solid-like features are added, while others are based on a solid-like starting point and incorporate liquid-like flow through flow defect mechanisms [22–24]. One example of a solid-like flow defect model is Shear Transformation Zone (STZ) Theory [16, 25], which has been applied to a wide range of amorphous materials, including metallic glasses [26–28], granular materials [29], and earthquake faults [30–33]. While STZ Theory has been successful in many situations, several of its ingredients remain poorly constrained by data, and further work is needed to assess the validity of many of its assumptions.

In this study, we apply STZ Theory to the deformation behavior of a Zr-based bulk metallic glass (Vit105) under compression. In particular, we focus on the temperature and strain rate dependence of plastic flow and aging behavior, for which a suite of experimental observations has been collected [13, 34–38]. We show that STZ Theory with a now incorporated temperature-dependent relaxation term captures the full range of experimental observations in a simple theoretical framework. We also demonstrate that STZ Theory provides a means of relating energy scales measured in experiments to the basic energy scales in the theory. The close match between experimental and theoretical results shows that STZ Theory is able to capture the deformation behavior of bulk metallic glasses over a broad range of temperatures and strain rates.

II. EXPERIMENTAL CHARACTERIZATION OF SHEAR BANDS IN METALLIC GLASSES

When subjected to an external load at ambient temperatures, metallic glasses deform plastically in a localized manner by the formation of shear bands [13–15], an example of which is shown in Fig. 1. At higher temperatures closer to the glass transition temperature, shear localization is typically not observed, and deformation occurs homogeneously throughout the sample.

Plastic deformation in shear bands can exhibit stick-slip behavior, also known as serrated

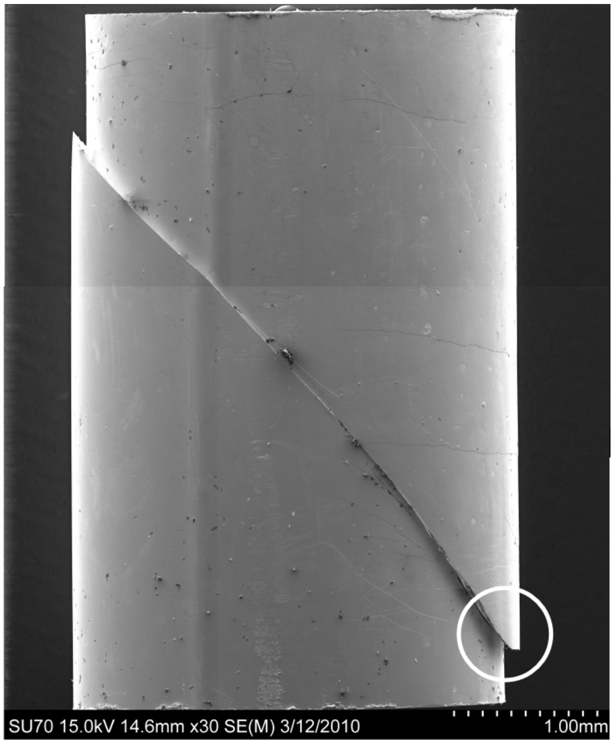

FIG. 1. SEM image of a bulk metallic glass sample following uniaxial compression. Plastic deformation occurred via a single shear band that intersects the surface of the sample. The shear offset can be observed at the sample edge, and is circled in the image.

flow (see Fig. 2(a)), where localized plastic deformation occurs intermittently with periods of slow elastic loading followed by rapid slip [13, 35, 39–43]. Stick-slip theory [44–46] shows that the rate dependence of the steady-state flow stress plays a central role in determining if stick-slip occurs. The rate dependence of the flow stress can be expressed mathematically through $m = d\sigma/d\dot{\gamma}$, where σ is the flow stress and $\dot{\gamma}$ is the strain rate. If $m < 0$, the material is rate-weakening and stick-slip can occur if the elastic stiffness of the system is sufficiently low. If $m > 0$, the material is rate-strengthening and stick-slip behavior cannot occur. For a Zr-based metallic glass, Dubach et al. [13, 43] performed a series of velocity step tests to explicitly measure the rate dependence of the flow stress. These tests showed that metallic glasses in the non-serrated flow regime exhibit rate-strengthening behavior, while tests in the serrated flow regime show rate-weakening behavior. Additionally, an Arrhenius scaling was observed for the transition from steady sliding to serrated flow as a function of strain rate and temperature, with an activation energy scale of 0.37 eV [13], as illustrated

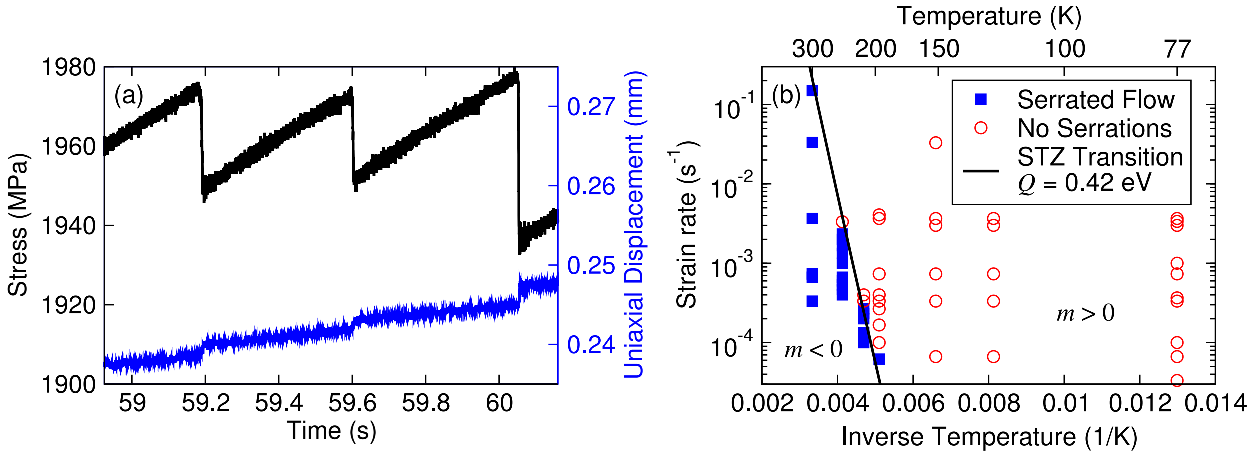

FIG. 2. (a) Serrated flow in a compression test of a Zr-based metallic glass sample at a strain rate of 10^{-3} s^{-1} and at room temperature [34]. The upper curve (vertical scale on the left) shows the evolution of the shear stress, with periods of slow elastic loading followed by periods of rapid slip. The lower curve (vertical scale on the right) shows the axial displacement, which confirms that the sample deformation is intermittent in time. (b) Map showing deformation type as a function of strain rate and inverse temperature [13]. Serrated flow occurs for high temperatures and low strain rates, and occurs when the material is rate-weakening ($m < 0$). At higher strain rates and lower temperatures, the material is rate-strengthening ($m > 0$) and no serrations are observed. The transition from serrated to non-serrated flow predicted by STZ Theory (details in Section V B) is shown with the solid line. In both the experiments and theory, the transition from steady sliding to serrated flow follows an Arrhenius scaling and shows a good match with the data. The activation energy from fitting the data is 0.37 eV, a good match with the value of 0.42 eV found from the theory.

in Fig. 2(b).

Additionally, slide-hold-slide experiments have been conducted to examine the static re-strengthening effect that occurs during the stick phase of serrated flow [38, 47] (see example experiment in Fig. 3(a)). These experiments generally show that the stress overshoot following a hold increases logarithmically with waiting time, and that the characteristic time scale for aging (that is, the waiting time at which non-zero stress overshoots are first observed) decreases as the temperature increases. By conducting tests at different temperatures, the underlying mechanism of shear band re-strengthening was shown to be thermally activated

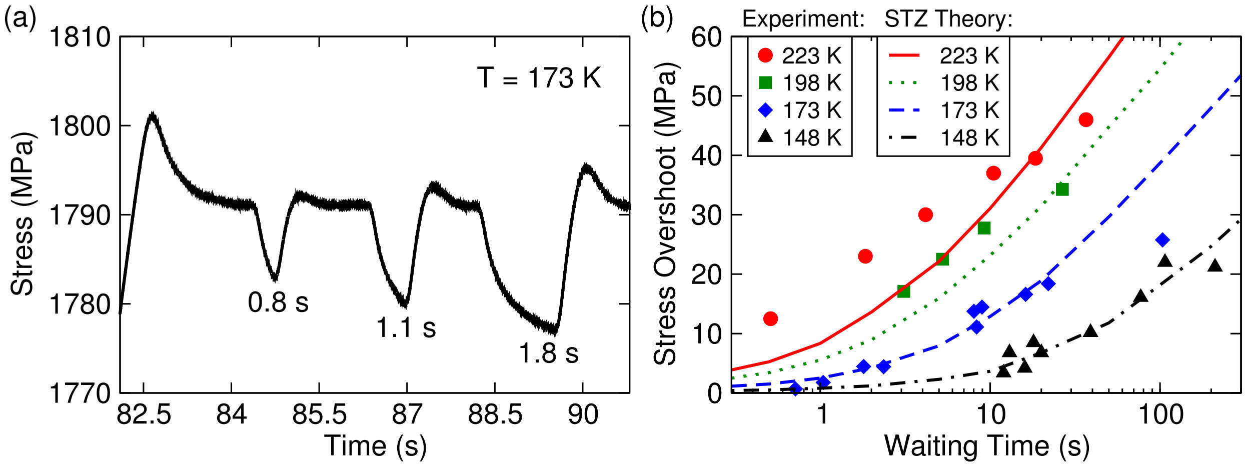

FIG. 3. (a) Example of a slide-hold-slide experiment at 173 K in the non-serrated flow regime [38, 47]. The plot shows stress as a function of time, with holds of 0.8 s, 1.1 s, and 1.8 s during the experiment. The stress has been de-trended to remove an overall decrease in flow stress with increasing strain. After each hold, the stress overshoots its steady-state value when shearing is re-started. (b) Stress overshoot as a function of waiting time. The overshoot grows logarithmically with time, and the characteristic time scale for aging varies with temperature, giving an energy scale of 0.16 eV. Predictions based on numerical integration of STZ Theory (lines; see details in Section IV) match the general aging behavior observed in the experiments (symbols).

with an activation energy of 0.16 eV [38, 47].

Temperature also plays a role in determining the flow stress in metallic glasses. Experiments show that metallic glasses exhibit a temperature-dependent flow stress at low temperatures. Various studies [12, 36, 43, 48, 49] have reported an increase in flow stress at low temperatures as large as 25% relative to the room temperature flow stress. These results are summarized in Fig. 4 and demonstrate that temperature influences the plastic flow of metallic glasses even far below the glass transition temperature.

In this work, we show that all of these experimental characteristics of plastic flow in metallic glasses, namely the thermally-activated aging behavior, the temperature-dependent flow stress, and the transition from serrated to non-serrated flow can be captured in an STZ model based on an effective disorder temperature. We develop a series of approximate solutions to the STZ equations to simplify the process of determining the STZ parameters from the data. Our results allow for a simplified integration of the experimental data with

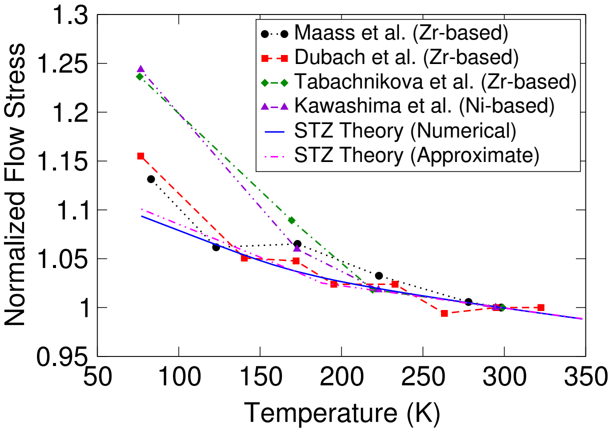

FIG. 4. Normalized flow stress as a function of temperature taken from several experimental studies of metallic glasses [36, 43, 48, 49]. STZ Theory predictions (for details see Section V A) are shown for the approximate solution (dot-dashed line) and numerical integration. STZ Theory follows the trends observed for the experimental data, and there is good agreement between the numerical and approximate STZ solutions. Each curve is normalized by the value at 298 K. At low temperatures, an increase in the value of the flow stress as large as 25% is observed.

the nonlinear STZ equations and provide a means for interpreting the variety of energy scales found in the experimental data.

III. STZ EQUATIONS

In this section we present the equations of STZ Theory, which we use in the following sections to provide a quantitative explanation of the experimental data in Section II. We first outline the basic ideas underlying STZ Theory, focusing in particular on the equations relevant for the bulk metallic glass experiments. More details on the complete set of STZ Equations, the thermodynamic arguments underlying the theory, and the various systems to which they have been applied can be found in a review by Falk and Langer [50].

In the bulk metallic glass experiments considered here, a 3 mm diameter cylindrical sample of length $l = 5$ mm is subjected to uniaxial compression. Elastic deformation occurs both due to elastic deformation of the sample and compliance of the experimental apparatus. Plastic deformation is accommodated in localized shear bands, and the stress evolves according to:

$$\frac{d\sigma}{dt} = \mu\left(\frac{\sqrt{2}\dot{\epsilon}l}{w} - \dot{\gamma}\right). \tag{1}$$

The effective elastic modulus (combining the elastic behavior of both the sample and the apparatus) is μ, $\dot{\epsilon}$ is the externally imposed strain rate, and $\dot{\gamma}$ is the plastic strain rate within the shear band, which evolves dynamically as the stress and effective temperature change. We assume that all plastic deformation occurs in the shear band, so that the effective externally imposed deformation rate in the shear band is $\sqrt{2}\dot{\epsilon}l/w$, with a shear band width $w = 2 \times 10^{-8}$ m [42, 51]. The factor of $\sqrt{2}$ corrects for the fact that the shear band is typically oriented at an angle of $\sim 45°$ relative to the compression axis of the sample (see Fig. 1). The elastic properties of the system do not affect the steady-state behavior, but they are important for transient stress dynamics such as stick-slip and transient loading in a slide-hold-slide experiment.

When describing the deformation of an amorphous material, the strain tensor is often split into affine (spatially homoegeneous) and non-affine (spatially heterogeneous) parts. The affine part usually occurs in an elastic manner, while the non-affine deformation can be either elastic or plastic in nature. In STZ Theory, the non-affine deformation is assumed to be entirely plastic, and non-affine strain occurs in localized regions that undergo rearrangement [16, 25]. These localized regions, or Shear Transformation Zones, occur when atoms rearrange from one metastable configuration to another. These zones have two distinct orientations, which we denote by "+" and "−", and the two orientations are aligned with the principal stress orientations in the material. Once a local zone is sheared into the "+" orientation, the zone cannot accumulate further plastic strain, so in order for the material to shear further, the "+" STZ must be destroyed, and a new "−" STZ must be created that can be sheared to accumulate additional plastic strain. Energy dissipation in the material constantly creates and destroys STZs, and as the material is sheared the plastic deformation reaches a steady-state where there is an appropriate balance between STZ creation, STZ destruction, and STZs rearranging from one orientation to the other. This steady-state number density follows a Boltzmann distribution with effective temperature χ [26], a temperature-like state variable describing configurational degrees of freedom in the amorphous system. Effective temperature has been measured in simulations of various amorphous materials [52], and is a dynamic quantity that evolves as the system deforms.

The effective temperature evolves slowly relative to the fast time scale over which the STZs are created and destroyed, and thus we assume that the number density of STZs is always at the steady-state value specified by the effective temperature.

Quantitatively, we can express the equations of STZ Theory based on two ingredients. First, we require an equation to relate the plastic strain rate to the rearrangement of STZs. The plastic strain rate $\dot{\gamma}$ is a function of the applied stress σ, the effective temperature χ, and the thermal temperature T as follows:

$$\dot{\gamma} t_0 = \epsilon_0 \exp\left(-\frac{Q^* - \sigma V^*}{kT} - \frac{1}{\chi} \right) \left(1 - \frac{\sigma_y}{\sigma} \right). \tag{2}$$

The plastic strain rate depends on the two factors in the exponential: the first is a thermally activated STZ rearrangement rate with a stress-dependent activation energy [53], and the other describes the density of STZs through the effective temperature [26]. The specific equation used here makes the additional assumption that backward STZ rearrangements (i.e. rearrangements where an STZ transitions from a "+" configuration to a "−" configuration) are rare and can be neglected. This approximation can be made because the applied stress is much larger than the stress scale for thermal activation, thus backward shearing events make a negligible contribution to the plastic strain rate.

The additional parameters are Boltzmann's constant k, the rearrangement attempt frequency $1/t_0$ (which should be similar to a molecular vibrational frequency), the typical number of atoms per STZ ϵ_0, the activation barrier for STZ rearrangements Q^*, and the STZ rearrangement activation volume V^*. The yield stress is indicated by σ_y, which is the stress below which all of the STZs are in the "+" orientation. For stresses lower than σ_y, there are no STZs which are oriented appropriately to deform plastically, thus $\dot{\gamma} = 0$ and no plastic deformation takes place. More details about the origin of this yield stress term can be found in several other papers on STZ Theory [46, 50, 54], though it does not play a significant role in the dynamics presented here.

Because the effective temperature is a dynamic quantity, the second required ingredient is an equation that describes the time evolution of the effective temperature. We assume that the effective temperature follows a heat equation, with terms for dissipation and relaxation [26, 55]. The evolution of the effective temperature is governed by the following equation:

$$\frac{d\chi}{dt} = \frac{\dot{\gamma}\sigma}{c_0 \sigma_y} \left(1 - \frac{\chi}{\hat{\chi}(\dot{\gamma})} \right) - R \exp\left(-\frac{Q}{kT} - \frac{\beta}{\chi} \right). \tag{3}$$

The effective temperature evolution equation contains two terms. The first is a dissipation term that drives the effective temperature towards its kinetically ideal value $\hat{\chi}$. The second term describes the relaxation of the effective temperature. The relaxation term has both a thermally activated factor and a factor dependent on the effective temperature that describes the number density of zones that can relax. Using a thermal contribution to the relaxation of effective temperature below the glass transition temperature has not been considered in previous studies using STZ Theory and we will show that this modification of Eq. (3) is key for explaining all of the experimentally observed phenomena in metallic glasses considered in this study. Other parameters in the effective temperature equation are a specific heat c_0, a relaxation rate R, an energy scale for forming relaxation zones β (scaled by the STZ formation energy), and the activation energy for relaxation events Q. For the kinetically ideal effective temperature, we choose a simplified form of the version used in Langer and Manning [56] based on simulations done by Haxton and Liu [57]:

$$\hat{\chi} = \frac{\chi_w}{\log\left(\frac{q_0}{\dot{\gamma} t_0}\right)}. \tag{4}$$

The steady-state effective temperature introduces two additional parameters: the normalized strain rate at which the steady-state effective temperature diverges q_0, and the normalized energy scale that determines the effective temperature rate dependence χ_w. Values for χ_w have been estimated based on simulation data, but experimental verification is more difficult as effective temperature cannot be measured directly. Part of the new contributions in this work is to show how the steady-state effective temperature can be constrained solely from experimental data.

STZ Theory introduces a number of parameters, some of which have been constrained based on physical arguments, while others have been fit using experimental and simulations results [26, 50, 56]. However, these previous efforts of fitting STZ Theory have either relied on data taken above the glass transition temperature to fit parameters that determine the viscosity curves [26], or numerical simulations that explicitly measure the effective temperature [56]. For metallic glass experiments at temperatures well below the glass transition temperature, these data are not available, and application of the theory needs to be independently verified using experimental results to see if the theoretical ideas that form the basis for the theory match experimental observations at low temperatures. In this study, we use a series of approximate solutions combined with numerical integration to perform this low-temperature analysis. Our study provides a new way to understand the dynamics of STZ Theory over a new range of experimental conditions not previously considered. In the sections that follow, we describe the essential results from our approximate solutions, the details of which can be found in the Appendix.

IV. AGING BEHAVIOR

First, we examine the dynamics of aging in STZ Theory, and compare the theory with aging data from slide-hold-slide experiments. Previous studies have examined the dynamics of slide-hold-slide experiments with STZ Theory [45, 58], and while these studies show some of the qualitative effects found in the experimental data, we examine the aging behavior quantitatively in this study. In a slide-hold-slide experiment, the sample is first sheared at a constant rate for sufficient time to reach a steady-state. Shearing is stopped temporarily to allow the system to age for a specified length of time, denoted by t_w, and shearing is then resumed. By measuring the transient dynamics of the stress when shearing resumes, we obtain quantitative information on the dynamics of aging during the hold.

An example of a series of slide-hold-slide tests calculated using STZ Theory is illustrated in Fig. 5. The thermal temperature is $T = 173$ K, the strain rate is $\dot{\gamma} = 10^{-3}$ s^{-1}, and holds of 1, 3, and 10 seconds occur during the test. Other parameters are given in Table I. The upper figure shows the stress as a function of time, and the lower figure shows the time evolution of the effective temperature. As can be seen from Fig. 5, during the hold, the stress and the effective temperature both relax with time away from their steady-state values. The effective temperature relaxes due to the relaxation term in the effective temperature equation of motion (Eq. (3)), while the stress relaxes due to continued plastic deformation (Eq. (1) with $\dot{\epsilon} = 0$). Upon reloading after the hold, there is a transient peak in the stress, and the size of this overshoot grows with the length of the hold. The peak in the stress occurs because the effective temperature relaxes during the hold – relaxation of the effective temperature decreases the number of STZs, and thus an increased stress is required to initiate plastic deformation when shearing is resumed.

An approximate solution to the time relaxation of the STZ equations (provided in Appendix A) allows us to derive an approximate expression for the stress overshoot following

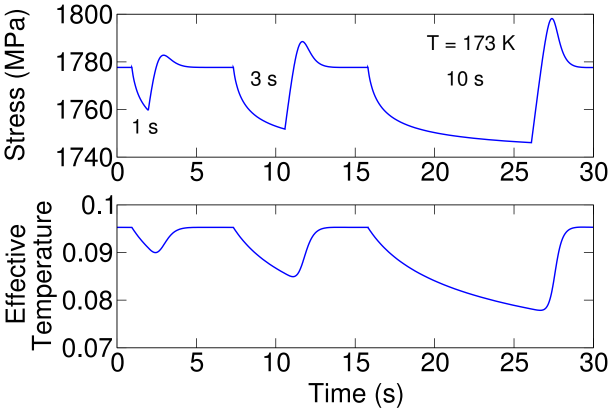

FIG. 5. Slide-hold-slide behavior of STZ Theory at $T = 173$ K and $\dot{\gamma} = 10^{-3}$ s^{-1}, with three holds of duration 1, 3, and 10 seconds starting at 1, 7.5, and 16 seconds, respectively. Parameters are given in Table I. The upper plot shows the evolution of the stress as a function of time, while the lower plot illustrates the dynamics of the effective temperature as a function of time. After each hold, the stress overshoots the steady sliding value, and the magnitude of this overshoot peak relative to the steady sliding stress quantifies the effect of aging. During each hold, both the stress and effective temperature relax, and then return to steady-state once deformation resumes.

a hold of length t_w:

$$\Delta\sigma = \frac{kT}{V^*\beta} \log\left(1 + t_w/\tau\right). \tag{5}$$

Here, τ is the characteristic time for the onset of effective temperature relaxation, determined from $\tau \approx \chi_{ss}^2/(\beta R \exp(-Q/kT - \beta/\chi_{ss}))$, where χ_{ss} is the steady-state effective temperature at the beginning of the hold. For holds of duration less than τ, the stress overshoot tends to zero. Changing the value of τ has the effect of moving the aging curves horizontally on a plot of $\Delta\sigma$ as a function of t_w.

This approximate solution reveals three important results regarding the aging behavior: (1) the stress overshoot $\Delta\sigma$ grows logarithmically with waiting time, (2) the stress overshoot tends to zero for holds less than the time scale τ, which scales with temperature as $\tau \propto \exp(Q/kT)$, and (3) the magnitude of the stress overshoot is proportional to $kT/(V^*\beta)$. Results (1) and (2) are directly confirmed by the experimental results in Fig. 3(b), which show a logarithmic increase in stress overshoot as a function of waiting time, as well as a horizontal shift in the stress overshoot curves as the temperature changes. The amount of this horizontal shift follows an Arrhenius scaling, and confirms the temperature dependence of the characteristic time τ, with $\tau \propto \exp(Q/kT)$ [47].

The solution in the appendix is only an approximation, as it ignores stress relaxation and the subsequent reloading that occur during a slide-hold-slide experiment. The solution assumes infinite stiffness while reloading, but due to the finite stiffness of the experimental apparatus, some plastic deformation occurs during re-loading. This means that the approximate solutions are an upper bound on the size of the stress overshoots, and we must explicitly account for the re-loading when comparing the theory to experiments. Thus, to make direct comparisons with the experimental data we numerically integrate the effective temperature evolution equation (Eq. (3)) and the stress evolution equation (Eq. (1)). To model the series of slide-hold-slide tests, the strain rate $\dot{\epsilon}$ is set to zero during the hold portions of the tests and set to 10^{-3} s^{-1} during the sliding portions of the tests. Parameters are given in Table I. The results from the numerical calculations are shown in Fig. 3(b), and confirm the general behavior found in the approximate solutions. The upper bounds from the infinite stiffness approximation for $\Delta\sigma$ in Eq. (5) are shown in Fig. 6. The infinite stiffness upper bounds are larger than the numerical results by as much as a factor of two, showing that the finite stiffness cannot be neglected. Agreement is very good between the experiments and the numerical results at low temperatures (Fig. 3(b)), while at higher temperatures the time scale τ in the theory deviates slightly from the time scale observed in the experiments. This is because the steady-state effective temperature decreases with increasing temperature at higher temperatures, introducing some additional temperature dependence into the theory that is not observed in the experiments.

One aspect of the experimental aging data that is not clear is whether the rate of increase of $\Delta\sigma$ with $\log(t_w)$ is temperature-dependent (i.e. if the slopes of the best fit lines to the experimental points of Fig. 3 vary with temperature). STZ Theory predicts that the slope should increase linearly with temperature, which can be seen in the results in Fig. 6. The experiments do not show a clear trend, because they were conducted over a range where T changes only by a factor of 1.5. Error bars on the experimentally determined stress overshoots are $\sim \pm 5$ MPa, so from the data it is not clear if the scaling between $\Delta\sigma$ and $\log(t_w)$ is temperature-dependent.

TABLE I. Parameter values for the bulk metallic glass data.

Parameter	Description
$t_0 = 10^{-13}$ s	STZ time scale
$\epsilon_0 = 10$	Number of atoms per STZ
$Q^* = 2.42$ eV	STZ rearrangement activation energy
$V^* = 1.97 \times 10^{-28}$ m^3	STZ rearrangement activation volume
$\sigma_y = 1$ GPa	Yield stress
$c_0 = 2 \times 10^4$	Effective temperature specific heat per unit volume (scaled by Boltzmann's constant times the yield stress divided by the STZ formation energy)
$q_0 = 1 \times 10^{-4}$	Strain rate at which the effective temperature diverges (scaled by the STZ time scale t_0)
$\chi_w = 1.5$	Energy scale for effective temperature rate dependence (scaled by STZ formation energy divided by Boltzmann's constant)
$R = 1 \times 10^6$ s^{-1}	Effective temperature relaxation rate
$Q = 0.16$ eV	Activation energy for relaxation events
$\beta = 0.9$	Energy scale for creation of relaxation events (scaled by STZ formation energy divided by Boltzmann's constant)
$\mu = 1.5 \times 10^{-4}$ GPa	Effective elastic modulus of apparatus and sample
$w = 2 \times 10^{-8}$ m	Shear band width
$l = 5$ mm	Sample length

V. STEADY-STATE BEHAVIOR

We now examine the temperature and rate dependence of the steady-state effective temperature χ under continuous shearing. In order to do this, we need to find the values of χ for which $d\chi/dt = 0$ at different temperatures and strain rates, based on the effective temperature evolution equation (Eq. (3)). While we focus on numerical solutions to this equation here, we also provide an approximate analytical solution for the steady-state effec-

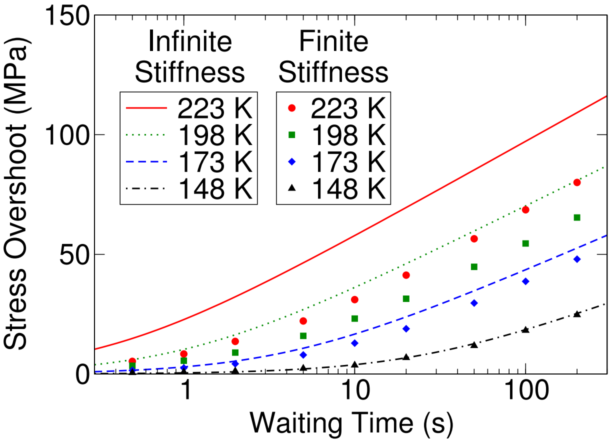

FIG. 6. Stress overshoots as a function of waiting time calculated from the approximate solution that assumes infinite stiffness of the system (lines), compared with numerical solutions (symbols) that account for the stiffness of the material and experimental apparatus. The approximate solution assumes infinite stiffness, and thus the approximate solution provides an upper bound on the size of the overshoot. The overshoots determined from the approximate solutions give a reasonable approximation for low temperatures, and show a larger discrepancy at high temperatures where the stress overshoots are larger.

tive temperature in Appendix B. This approximate solution is given by:

$$\frac{1}{\chi} = \begin{cases} \frac{1}{\hat{\chi}} & T < T_c \\ \frac{1}{\hat{\chi}} - \frac{Q}{k\beta}\left(\frac{1}{T} - \frac{1}{T_c}\right) & T \geq T_c \end{cases}, \tag{6}$$

where T_c is the characteristic temperature that separates the two regimes,

$$T_c = \frac{Q}{k}\left\{\log\left[\frac{Rc_0\sigma_y \exp\left(-\beta/\chi_c\right)}{\dot{\gamma}\sigma(1-\chi_c/\hat{\chi})}\right]\right\}^{-1}, \tag{7}$$

where χ_c is a crossover effective temperature, given by $\chi_c = \beta((1+4\hat{\chi}/\beta)^{1/2} - 1)/2$. In the low-temperature regime, the steady-state effective temperature is independent of temperature, whereas at high temperatures, the steady-state effective temperature decreases with increasing thermal temperature. The steady-state effective temperature is also dependent on strain rate, as $\hat{\chi}$ and T_c are both dependent on strain rate. For low temperatures, we see a weaker dependence of the effective temperature on strain rate, while at higher temperatures the strain rate dependence of the effective temperature is stronger. Fig. 7 illustrates these two regimes in a plot of $\exp(-1/\chi)$ as a function of inverse temperature, with different curves representing different strain rates.

These two regimes can be qualitatively understood by inspecting Eq. (3). In the limit of very low temperatures, the relaxation term becomes small, such that the effective temperature tends to its kinetically ideal value $\hat{\chi}$ as given by the data of Haxton and Liu [57]. At higher temperatures, relaxation sets in. Consequently, the steady-state effective temperature begins to deviate from $\hat{\chi}$ and the effective temperature decreases with increasing thermal temperature. The exact temperature at which the crossover between the low- and high-temperature regimes occurs varies with the strain rate. All of these qualitative aspects of the steady-state effective temperature are confirmed in the approximate analytical solution. The approximate solution also confirms the strain rate dependence of the crossover temperature between these two regimes. As will be shown in the following, the crossover between the different regimes of steady-state effective temperature as a function of temperature and strain rate turns out to be the fundamental phenomenon behind the experimentally observed increase in flow stress at low temperatures as well as the transition between serrated and non-serrated flow (or rate-weakening and rate-strengthening).

A. Steady-State Flow Stress

The temperature and strain rate dependencies of the effective temperature have several consequences for the dynamics of plastic flow. First, one can show that the steady-state flow stress is temperature-dependent. Using the approximate solution for the effective temperature, the corresponding steady-state flow stress is

$$\sigma = \begin{cases} \frac{Q^*}{V^*} + \frac{kT}{V^*}\left(\log\left(\frac{\dot{\gamma}t_0}{\epsilon_0}\right) + \frac{1}{\hat{\chi}}\right) & T < T_c \\ \frac{Q^* - Q/\beta}{V^*} + \frac{kT}{V^*}\left(\log\left(\frac{\dot{\gamma}t_0}{\epsilon_0}\right) + \frac{1}{\hat{\chi}} + \frac{Q}{k\beta T_c}\right) & T \geq T_c \end{cases}, \tag{8}$$

with T_c as defined above. This result is discussed in more detail in Appendix C. As with the solution for the steady-state effective temperature, there are two regimes: a low-temperature regime where the steady-state effective temperature is independent of thermal temperature, and a high-temperature regime where the steady-state effective temperature changes with thermal temperature. In the low-temperature regime, we find that the shear stress is more strongly dependent on temperature than at high temperatures, which is illustrated in Fig. 4. The approximate solution assumes that there is an abrupt transition between these two regimes, but in the numerical solution the transition is more gradual. However, as shown

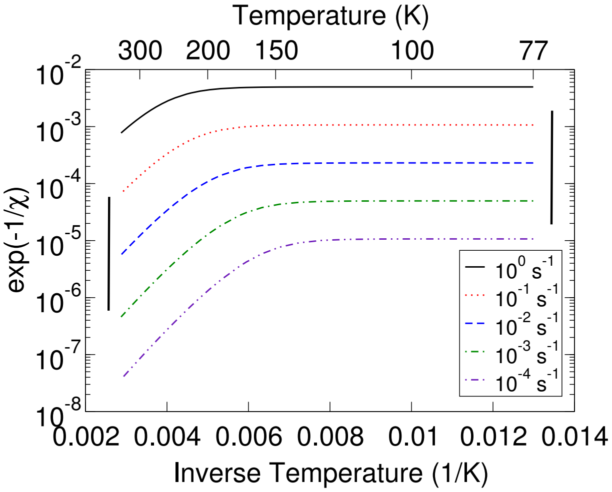

FIG. 7. Strain rate and temperature dependence of the steady-state effective temperature. The plot shows $\exp(-1/\chi)$ as a function of the inverse temperature for different values of the strain rate, with the temperature specified on the upper horizontal axis. At a fixed strain rate, the effective temperature is constant as a function of temperature for low temperatures, while the effective temperature decreases with increasing temperature at high temperatures. This is because the relaxation rate is strongly temperature-dependent – at low temperatures relaxation is weak and $\chi = \hat{\chi}$, while at high temperatures relaxation leads to a steady-state value that is smaller than $\hat{\chi}$. The temperature at which the effective temperature changes from being temperature-independent to temperature-dependent varies with strain rate, occurring at a higher temperature for higher strain rates. This behavior is central to determining the rate dependence of steady flow, as at low temperatures the steady-state stress is rate-strengthening, while at high temperatures the steady state stress is rate-weakening. The rate dependence can be observed by noting that for a two decade increase in the strain rate, $\exp(-1/\chi)$ increases by less than two decades at low temperatures, whereas a two decade increase in the strain rate causes $\exp(-1/\chi)$ to increase by more than two decades at high temperatures (the vertical lines at the sides illustrate a two decade change in $\exp(-1/\chi)$). This explains why serrated flow is seen at higher temperatures, as a rate-weakening behavior is required for stick-slip instabilities to occur, and why the strain rate at which flow transitions from serrated to non-serrated flow is temperature dependent.

in Fig. 4, the approximate and numerical solutions are in close agreement with one another even near the temperature at which the transition between the two regimes occurs.

Physically, the shear stress is more strongly dependent on temperature at low temperatures because of the interplay between the temperature dependence of the effective temperature and the thermal activation of STZ rearrangements. In the low-temperature regime, the effective temperature is independent of thermal temperature. Thus, if the thermal temperature increases, there is no change in the number of STZs. However, because thermal activation of STZ rearrangements is enhanced, the flow stress decreases because the STZs rearrange at a faster rate. Therefore, at low temperatures the flow stress decreases linearly with increasing temperature.

At higher temperatures, the effective temperature is itself dependent on the thermal temperature, and the behavior changes. An increase in the thermal temperature still enhances thermal activation of STZ rearrangements, but because the effective temperature decreases as the thermal temperature increases, there are fewer STZs. Thus, the decrease in the number of STZs mitigates the thermal activation effect, and we expect to see a weaker dependence of the steady-state flow stress on temperature. The scaling remains linear, though with a smaller slope than is found at low temperatures.

These two different regimes are observed in experiments, as shown in Fig. 4, which illustrates the temperature dependence of the flow stress in STZ Theory compared with the metallic glass data [36, 43, 48, 49]. At low temperatures there is a strong dependence of the flow stress on temperature, while at higher temperatures the flow stress has a temperature dependence that is weaker. The predictions of STZ Theory compare favorably with the experiments. A previous study by Johnson and Samwer [59] showed that the bulk metallic glass flow stress scales approximately with $T^{2/3}$. In the STZ equations presented here, we find that there are two regimes, each with a linear scaling between flow stress and temperature, but with two different slopes. Because the slopes in these two regimes differ, the overall scaling between the flow stress and the temperature across both regimes will be weaker than linear, with a scaling exponent similar to the 2/3 observed in the data. Thus, we find that the temperature dependence of both thermal activation of STZs and changes in the STZ density provide an explanation for the scaling observed in the Johnson and Samwer study.

B. Transition to Serrated Flow

Another consequence of the temperature and strain rate dependence of the effective temperature is the transition between serrated and non-serrated flow. Experiments show that bulk metallic glasses deform via steady sliding at low temperatures and high strain rates, while flow exhibits stick-slip behavior at high temperatures and low strain rates [13, 35]. Here, we show how this transition arises from the temperature and strain rate dependence of the steady-state effective temperature. We also show that this transition exhibits an Arrhenius scaling in STZ Theory, which is confirmed by the experiments [13].

In STZ Theory, the rate dependence of the steady-state flow stress is mathematically represented by $m = d\sigma/d\dot{\gamma}$. As is shown in Fig. 7, the steady-state effective temperature always increases with increasing strain rate. However, the steady-state flow stress can either increase or decrease with increasing strain rate, depending on how quickly the steady-state effective temperature increases with strain rate (see Eq. (2)). If the steady-state effective temperature (or more precisely, the factor $\exp(-1/\chi)$) increases more slowly than the strain rate, a counterbalancing effect requires an increase in the flow stress to raise the rate of STZ rearrangements to maintain the prescribed strain rate. This effect leads to steady-state rate-strengthening behavior ($m > 0$). However, if $\exp(-1/\chi)$ increases more quickly than the strain rate, the shear stress decreases with increasing strain rate and the material will exhibit rate-weakening behavior ($m < 0$). More detailed calculations regarding the rate dependence of the steady-state flow stress are provided in Appendix D.

The rate dependence of the flow stress in STZ Theory can therefore be determined by examining Fig. 7. At low temperatures, as the strain rate is increased by a decade, the factor $\exp(-1/\chi)$ does not increase by a decade. This is explicitly denoted at the far right of the plot, where a line indicating two decades on the vertical scale is drawn. This means that the steady-state flow stress exhibits rate-strengthening behavior at low temperatures. However, at high temperatures, where the steady-state effective temperature is temperature-dependent, $\exp(-1/\chi)$ increases by more than a decade with a decade increase in strain rate. This can be seen explicitly by comparing a two decade change in the strain rate with the vertical line indicating a two decade change in $\exp(-1/\chi)$ at the far left of the plot. This illustrates that in the STZ equations presented here, there is a transition from rate-strengthening behavior at low temperatures to rate-weakening behavior at high temperatures. Additionally, as the strain rate increases, the transition between the two regimes occurs at successively higher temperatures.

This result explains why serrated flow occurs in metallic glasses at high temperatures and low strain rates, and no serrated flow occurs at low temperatures and high strain rates. Because rate-weakening behavior is required for stick-slip to occur [44–46], serrated flow occurs in the rate-weakening regime at high temperatures, and non-serrated flow occurs in the rate-strengthening regime at low temperatures. There is also a strain rate dependence in this transition: at low strain rates, we find that the transition temperature between the two regimes is lower when compared to higher strain rates. Thus, there is a greater range of temperatures where serrated flow occurs at low strain rates.

To confirm this qualitative picture, we explore the details of this transition in the STZ equations quantitatively by calculating where the rate-strengthening to rate-weakening transition occurs as a function of temperature and strain rate. This calculation is provided in Appendix D, with the end result being that we expect the rate-strengthening to rate-weakening transition to exhibit an Arrhenius scaling. The energy scale for this transition depends on the other energy scales introduced in the theory: the relaxation activation energy Q, the relaxation energy scale β, which is the energy scale for creating a configuration that can relax, and χ_w, the energy scale controlling how the kinetically ideal effective temperature $\hat{\chi}$ changes with strain rate. The latter two of the three energy scales (β, χ_w) are normalized by the STZ formation energy in the theory, so the STZ creation energy also plays a role in determining the energy scale of the rate-strengthening to rate-weakening transition. Using the parameters in Table I, we calculate that the activation energy for the transition from stick-slip to steady sliding is $\approx 3Q = 0.48$ eV (see Appendix D). Numerical calculations using the STZ equations give a value of 0.42 eV for this energy scale, as illustrated in Fig. 2(b). This shows good agreement with the experimental data from bulk metallic glasses [13], as well as numerical calculations estimating the energy scale of STZ rearrangements [60, 61].

One important result from the comparisons between experiment and theory is that the energy scale for the rate-strengthening to rate-weakening transition is not a simple input into the theory, but rather an energy scale that results from several different physical processes. Conversely, it also shows that while experiments may not be able to directly measure all of the energy scales that are inputs to theory (i.e. while the experiments can determine Q, the energy scales β and χ_w are not directly measured), the dynamics of the serrated to non-serrated flow transition can determine these other energy scales. Therefore, close interaction between experiments and theory is necessary to assess experimental results and determine their consequences for theories of how amorphous materials deform and fail.

VI. DETERMINING PARAMETER VALUES

We use the approximate solutions discussed above to constrain the parameters that match the experimental metallic glass data presented in Table I. First, we use physical estimates for the STZ time scale t_0 and atoms per STZ ϵ_0. The STZ time scale is on the order of atomic vibration frequencies of 10^{-13} s. Different versions of STZ Theory interpret ϵ_0 in slighly different ways, and the value of this parameter ranges from unity to 10 in various studies with STZ Theory [26, 62]. We choose $\epsilon_0 = 10$, which is on the large end of this range, since the experiments in question are 3D and each STZ should involve more atoms than in 2D. Because of the strong exponential dependence of the strain rate on stress, the value for ϵ_0 only needs to be an order of magnitude estimate; a large change in ϵ_0 leads to only a small change in the steady-state flow stress and has a minimal effect on the dynamics. The activation volume V^* is estimated from experimental data, and is taken to be 200 atomic volumes [43]. The yield stress plays no role in the dynamics considered here as long as it is below the flow stresses in question, and we choose a value of 1 GPa.

The remaining parameters are estimated from the experiments through the following steps. First, we recognize from the approximate solutions that the activation energy for relaxation events Q is the same as the value that is extracted from the experiments. Next, we estimate the normalized energy scale for creation of relaxation events to be $\beta = 0.9$. This value is chosen to be less than unity so that the flow stress has a negative rate dependence at higher temperatures, a requirement for stick-slip to occur. Smaller values of β are possible, but we expect the energy scale for formation of relaxation events to be similar to the STZ formation energy.

Once β has been chosen, all other parameters are constrained from application of the approximate solutions to the experimental data. Using the approximate steady-state flow stress curve, we estimate the crossover temperature to be $T_c = 190$ K at $\dot{\epsilon} = 10^{-3}$ s^{-1}. Using the flow stress data at temperatures above T_c and the equivalent equation in the approximate solution (Eq. (8)), we can use the absolute value of the flow stress and its linear dependence on temperature to determine the STZ activation energy Q^* and the kinetically ideal effective temperature $\hat{\chi}$. From the data, a typical flow stress at 298 K is 1.7 GPa, increasing by about 4% at 200 K, allowing us to calculate $\hat{\chi} = 0.1$ and $Q^* = 2.42$ eV.

Next, with the value of $\hat{\chi}$ fixed, we determine the relaxation rate R. Using the time scale for relaxation τ, which is determined from the experiments at 173 K, we can determine R. We estimate the waiting time at 173 K to be 4 s, giving $R = 10^{-6}$ s^{-1}. Next, we use the equation that defines the crossover temperature (Eq. (7)) to solve for the effective temperature specific heat $c_0 = 2 \times 10^4$.

The final step is to determine χ_w and q_0, which set the kinetically ideal effective temperature $\hat{\chi}$. This is done using the activation energy for the transition from serrated to non-serrated flow, Eq. (D15), which depends on χ_w and the previously constrained parameters. In practice, the value of χ_w in Table I differs slightly from the value found from the approximate solution. An activation energy of 0.37 eV gives $\chi_w = 1.9$ using Eq. (D15), though we find $\chi_w = 1.5$ gives a better fit to the experimental data for the stick-slip to steady sliding transition due to the approximate nature of the analytical solution. This value matches the value derived for the Haxton and Liu data [56].

The method for deriving parameters described here is a way to estimate the STZ parameters using low-temperature data. In particular, it provides a way to estimate the steady-state effective temperature and its rate dependence directly from the experiments, which provides an independent confirmation of effective temperature estimates based on numerical simulations. Our method also provides a complementary approach to the fitting procedures used for data above the glass transition temperature [26]. As more experimental data for various metallic glasses is collected over a range of temperatures, both methods for estimating parameters should prove valuable in examining the ability of STZ Theory to capture additional aspects of failure and deformation over a range of conditions.

VII. DISCUSSION

This study shows that STZ Theory can capture several experimental observations of the deformation of bulk metallic glasses in a consistent theoretical framework. We find that a temperature-independent dissipation term and a temperature-dependent relaxation term in the effective temperature evolution can explain diverse features of the observed deformation behavior as a function of strain rate and temperature. While some of the individual aspects of metallic glass deformation have been studied separately in previous studies (i.e. aging, steady-state flow, and the steady sliding to stick-slip transition), our study integrates several types of experiments at different temperatures and strain rates and demonstrates quantitative agreement in a variety of contexts. Our identification of relaxation as a mechanism for producing rate-weakening behavior, while the dissipation term produces rate-strengthening behavior, resolves previous disagreements between STZ Theory and velocity step experiments [13] that showed both rate-weakening and rate-strengthening behavior at different temperatures. Previous version of STZ Theory have shown that the model is either rate-strengthening or rate-weakening [31, 54, 63], and simulations tend to show rate-strengthening behavior [56, 57]. Further, the behavior of the dissipation and relaxation terms over different temperature and strain rate regimes goes beyond explaining the rate dependence and simultaneously matches the stress overshoot and steady-state stress observations in a quantitative fashion.

Many of the parameters in the theory can be estimated on physical grounds, and the others are constrained directly from the experimental data. We find that our parameter values are generally consistent with other studies using STZ Theory [26, 62]. One difference that we find is that our value for the specific heat c_0 is larger by several orders of magnitude when compared to values used in previous studies of deformation of bulk metallic glasses, where it is found to be of order unity [26]. The previous works focused on deformation of metallic glasses at higher temperatures, much closer to the glass transition temperature, where deformation tends to be more homogeneous throughout the sample rather than localized to a narrow shear band. Therefore, it is possible that the differing values of the specific heat parameter are due to different temperature regimes and deformation types. Because the specific heat parameter plays a central role in determining the transient dynamics of deformation, further studies investigating the details of the transient dynamics of aging and stick-slip are required to better understand the specific heat parameter and whether its value changes with the type of deformation. We have conducted preliminary numerical studies that suggest that $c_0 = 2 \times 10^4$ gives transient overshoots that are too slow to match the observed transient stress overshoots in the Vit105 data examined here. However, studies with $c_0 \approx 1$, consistent with the high temperature data near the glass transition temperature, produce transients that are much faster than the observed low-temperature behavior and the stress overshoots are much smaller than those observed in the experiments. Further work to investigate the issue of transient dynamics is part of ongoing work.

In a recent paper, Sun et al. [63] used a version of STZ Theory to explore the transition from serrated to non-serrated flow. In their work, the transition from serrated to non-serrated flow occurs due to a different mechanism than in our work. In the Sun et al. paper [63], the effective temperature evolves only due to dissipation and the rate dependence of the steady-state flow stress is always assumed to be rate-weakening. In that case, the transition between serrated and non-serrated flow occurs because of a critical stiffness. At stiffnesses below the critical stiffness, steady sliding is unstable to perturbations and the system deforms through serrated flow. In our work, the transition from stick-slip to stable sliding occurs due to a competition between dissipation and relaxation leading to a change from steady-state rate-strengthening to steady-state rate-weakening. The stiffness also plays a role in determining the stick-slip to steady sliding transition in our model, but for the 3 mm diameter samples considered here, the samples are relatively compliant (larger samples have a reduced stiffness), ensuring that the elastic stiffness is smaller than the critical stiffness for all of the experiments considered here.

We believe that several experimental and computational results support our model of the serrated to non-serrated flow transition. First, the aging experiments show that during a hold in a slide-hold-slide experiment, there is a time-dependent relaxation of the effective temperature leading to a temperature-dependent stress overshoot when sliding restarts after the hold. If we assume the absence of a thermally activated relaxation term (i.e. $R = 0$ in Eq. (3)), the stress overshoot behavior does not match the temperature dependence of the onset time scale τ observed in the experiments. Second, Dubach et al. [13, 43] conducted explicit measurements of the rate dependence of the flow stress via velocity stepping experiments. They found that the metallic glasses exhibit rate-strengthening behavior when non-serrated flow occurs, in agreement with our model. Finally, the steady-state effective temperature used in both this study and the Sun et al. [63] study is based on simulations done by Haxton and Liu [57], where the effective temperature can be measured. In those simulations, rate-strengthening behavior was observed, and Langer and Manning [56] were able to determine a value of $\chi_w = 1.5$ to fit the simulations, a value consistent with rate-strengthening behavior. We find that this value of χ_w provides a good fit to the metallic glass data in this study.

STZ Theory is able to match a variety of experimental observations over many temperatures and strain rates. These comparisons are able to constrain many parameters in the theory, particularly the energy scales for various types of rearrangements. However, it remains to be determined what these energy scales are from first principles, and whether the picture provided here where each of these energy scales is a constant suffices to capture all essential features of plastic deformation. STZ Theory has been extended to consider a range of energy barriers for plastic rearrangements [64, 65] (rather than the assumption here of a single energy scale for rearrangements). While our work did not require a distribution of energy barriers for plastic rearrangements, future work will examine this possibility and if the predictions match the experimentally observed deformation behavior.

Our work confirms the experimental observation that there are many relevant energy scales in the deformation of a bulk metallic glass, and the theory provides a means to interpret and understand the experimental observations. In particular, we show that the energy scale derived from the aging experiments is the same as the activation energy for STZ relaxation in the theory, but that the energy scale derived from the critical strain rate is a complicated combination of several other energy scales. This shows that it is difficult to directly measure energy scales in a complicated system such as a glass, and that a combination of experiments with a predictive theory is needed to make sense of experimentally measured energy scales. Future efforts must continue to perform experiments in conjunction with theory in order to better understand how metallic glasses deform and fail over a range of temperatures and strain rates. This avenue of research is essential for understanding the basic physics of deformation of amorphous materials, and the further pursuit of this complex problem is needed to develop theories based on first principles with predictive power, theories that will with no doubt enhance the use of amorphous materials in a wide range of materials applications.

Appendix A: Approximate Solution for Aging Dynamics

In order to gain insight into the aging behavior of the STZ model, we find an approximate solution to the relaxation of the effective temperature. During relaxation, the effective temperature is governed by the differential equation:

$$\frac{d\chi}{dt} = -R\exp\left(-Q/kT - \beta/\chi\right). \tag{A1}$$

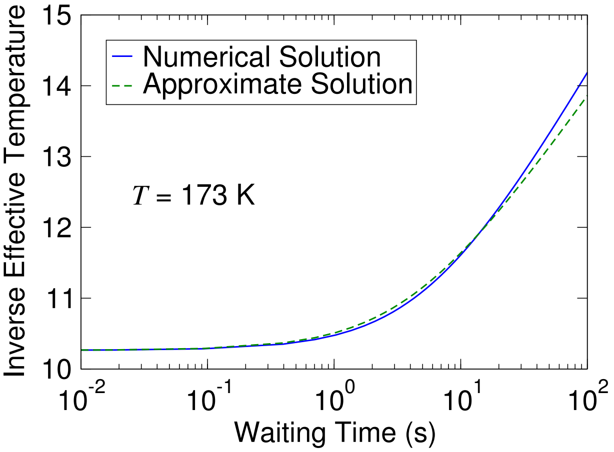

FIG. 8. Comparison between the approximate solution and numerical integration for metallic glass aging at 173 K. At $T = 173$ K, the characteristic time scale for relaxation is $\tau = 4.09$ s. The approximate solution provides a good fit to the solution obtained through numerical integration. Parameters are given in Table I.

The initial value of the effective temperature is the steady-state value. Here, we assume that the plastic strain rate is negligible during a hold. Because we observe stress relaxation during the hold in the experiments, the experimental plastic strain rate is nonzero, and thus these calculations provide an upper bound on the magnitude of the effective temperature relaxation and stress overshoot during an experiment.

We find that an approximate solution for χ is

$$\frac{1}{\chi(t)} = \frac{1}{\chi_{ss}} + \frac{1}{\beta}\log\left(1 + t/\tau\right), \tag{A2}$$

with τ representing a characteristic onset time for effective temperature relaxation. We estimate $\tau \approx \chi_{ss}^2/(\beta R \exp(-Q/kT - \beta/\chi_{ss}))$, which is the characteristic time scale for effective temperature relaxation determined from the Jacobian of the STZ equations (precisely, this time scale is the multiplicative inverse of the derivative of $d\chi/dt$ with respect to χ). We note that this time scale scales with temperature as $\tau \propto \exp(Q/kT)$. A comparison between this approximate solution and a numerical solution is shown in Fig. 8. The approximate solution compares favorably to the result obtained by numerical integration.

Using the solution for χ, we can calculate the stress overshoot as follows. We assume that there is little effective temperature evolution during re-loading following the hold, due to a small plastic strain rate during reloading. This is not exactly true, and thus the calculations here give an upper bound on the size of the stress overshoot. The value of the effective temperature at the peak stress σ_p is then the same as at the end of the hold, which we denote by $\chi(t_w)$. Since the time derivative of the stress at the peak is zero, the plastic strain rate must be the same as the effective driving rate, or $\dot{\gamma} = \sqrt{2}\dot{\epsilon}l/w$, at the peak stress. The plastic and effective driving rates must also be equal at steady-state, meaning that we can write

$$-\frac{Q^* - \sigma_p V^*}{kT} - \frac{1}{\chi(t_w)} = -\frac{Q^* - \sigma_{ss} V^*}{kT} - \frac{1}{\chi_{ss}}. \tag{A3}$$

Since the stress overshoot is $\Delta\sigma = \sigma_p - \sigma_{ss}$, this becomes

$$\Delta\sigma = \sigma_p - \sigma_{ss} = \frac{kT}{V^*}\left(\frac{1}{\chi(t_w)} - \frac{1}{\chi_{ss}}\right). \tag{A4}$$

Using the approximate solution for $\chi(t_w)$, we find that

$$\begin{aligned}\Delta\sigma &= \frac{kT}{V^*}\left(\frac{1}{\chi_{ss}} + \frac{1}{\beta}\log\left(1 + t_w/\tau\right) - \frac{1}{\chi_{ss}}\right) \\ &= \frac{kT}{V^*\beta}\log\left(1 + t_w/\tau\right). \end{aligned} \tag{A5}$$

This expression predicts a logarithmic increase in the stress overshoot with time, as is observed in the bulk metallic glass aging experiments. The experiments also show that the characteristic onset time τ should scale with temperature in an inverse Arrhenius fashion (i.e. $\tau \propto \exp(Q/kT)$), confirming our assumption that the relaxation term is thermally activated. This correspondence allows us to identify the experimentally observed activation energy of 0.16 eV as the activation barrier Q for relaxation events in the STZ equations.

Because these calculations assume that the plastic deformation during the hold and reload is negligible, they give an upper bound on the size of the stress overshoot. In practice the stress overshoots are smaller when calculated numerically. For the sake of making comparisons with the experimental data, we use the numerical simulation results in the main text.

Appendix B: Approximate Steady-State Solution

To examine the steady-state behavior, we find an approximate steady-state solution for the effective temperature. The nonlinear differential equation governing the evolution of the effective temperature cannot be solved in closed form, but we find an approximate solution that captures the essential regimes and can be useful for comparing with experiments. The effective temperature evolves according to

$$\frac{d\chi}{dt} = \frac{\dot{\gamma}\sigma}{c_0\sigma_y}\left(1 - \frac{\chi}{\hat{\chi}(\dot{\gamma})}\right) - R\exp\left(-\frac{Q}{kT} - \frac{\beta}{\chi}\right), \tag{B1}$$

and we would like to determine the value of χ for which $d\chi/dt = 0$ as a function of temperature and strain rate. Since the relaxation term depends exponentially on the effective temperature, while the dissipation term has a linear dependence on the effective temperature, a first order approximation can be found by solving for the effective temperature in the exponential:

$$\begin{aligned} \exp\left(-\beta/\chi\right) &= \frac{\dot{\gamma}\sigma}{Rc_0\sigma_y}\left(1 - \frac{\chi}{\hat{\chi}}\right)\exp\left(Q/kT\right) \\ \Rightarrow \frac{1}{\chi} &= -\frac{1}{\beta}\left(\frac{Q}{kT} + \log\left[\frac{\dot{\gamma}\sigma}{Rc_0\sigma_y}\left(1 - \frac{\chi}{\hat{\chi}}\right)\right]\right). \end{aligned} \tag{B2}$$

Our approximation assumes that $\log[\sigma(1-\chi/\hat{\chi})]$ is relatively constant over the temperature range in question, and that the temperature is large enough that relaxation cannot be neglected (otherwise, $\chi = \hat{\chi}$ and the logarithm is not defined). This suggests that we can construct a solution with $\chi = \hat{\chi}$ in the low-temperature regime and χ given by Eq. (B2) in the high-temperature regime, with a crossover at T_c:

$$\frac{1}{\chi} = \begin{cases} \frac{1}{\hat{\chi}} & T < T_c \\ \frac{1}{\hat{\chi}} - \frac{Q}{k\beta}\left(\frac{1}{T} - \frac{1}{T_c}\right) & T \geq T_c \end{cases}. \tag{B3}$$

The crossover temperature T_c can be determined by differentiating Eq. (B2) with respect to the inverse temperature, which yields

$$\begin{aligned} \frac{d(1/\chi)}{d(1/T)} &= -\frac{Q}{\beta k} - \frac{\chi^2/\hat{\chi}}{\beta\left(1 - \chi/\hat{\chi}\right)}\frac{d(1/\chi)}{d(1/T)} \\ \Rightarrow \frac{d(1/\chi)}{d(1/T)} &= -\frac{Q}{\beta k}\left[1 + \frac{\chi^2}{\beta\left(\hat{\chi} - \chi\right)}\right]^{-1}. \end{aligned} \tag{B4}$$

This expression confirms our approximate solution. If $\chi = \hat{\chi}$, the effective temperature is independent of thermal temperature, as $d(1/\chi)/d(1/T) = 0$. If the effective temperature is small relative to $\hat{\chi}$, then the inverse effective temperature scales linearly with the inverse temperature, since $d(1/\chi)/d(1/T) = -Q/(\beta k)$. The crossover between these two regimes thus can be estimated by defining a crossover effective temperature χ_c at which the two terms in square brackets in Eq. (B4) are equal. Thus, χ_c is defined by $\chi_c^2 = \beta(\hat{\chi} - \chi_c)$ or

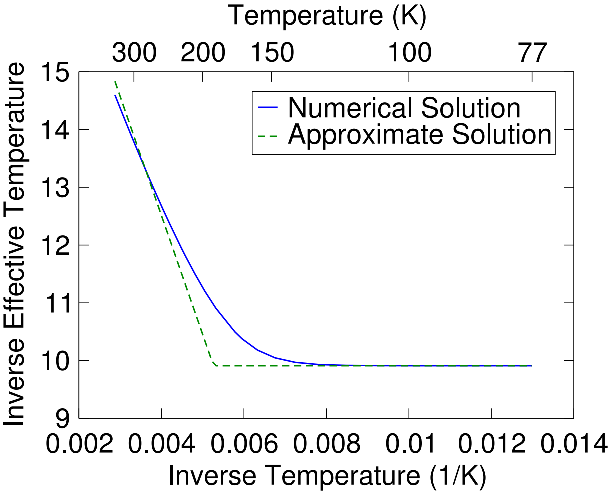

FIG. 9. Comparison between the approximate steady-state solution and the steady-state solution found by numerical integration as a function of temperature. The strain rate is 10^{-3} s^{-1}, at which the crossover temperature is $T_c = 190$ K. Parameters are given in Table I.

$\chi_c = \beta((1 + 4\hat{\chi}/\beta)^{1/2} - 1)/2$. The corresponding crossover temperature T_c can be found by solving Eq. (B3) for the temperature at which $\chi = \chi_c$. The result is

$$T_c = \frac{Q}{k}\left\{\log\left[\frac{Rc_0\sigma_y \exp\left(-\beta/\chi_c\right)}{\dot{\gamma}\sigma(1-\chi_c/\hat{\chi})}\right]\right\}^{-1}. \tag{B5}$$

This temperature designates where relaxation begins to play an important role in determining the steady-state effective temperature. Note that the temperature T_c exhibits an approximately logarithmic dependence on the strain rate, indicating that the crossover temperature increases as the strain rate increases. This confirms the behavior found in numerical calculations, which we present in Fig. 7 in the main text.

To confirm that this solution approximates the steady-state effective temperature, we compare results of numerically integrating the STZ equations with the approximate solutions. Fig. 9 shows the effective temperature found by Eq. (B4) and compares it to the result found by numerically integrating Eq. (B2). The approximate solution is in good agreement with the data obtained from numerical integration. The two solutions differ by the greatest amount when $T \approx T_c$, as the approximate solution assumes a sudden transition from one regime to the other, while the numerical solution exhibits a more gradual transition between the two regimes.

Appendix C: Approximate Steady-State Flow Stress

Using the approximate solution for the steady-state effective temperature, we can examine the temperature dependence of the steady-state flow stress. Using the equation for the plastic strain rate, we can express the shear stress in terms of the strain rate and effective temperature:

$$\sigma = \frac{Q^*}{V^*} + \frac{kT}{V^*}\left(\log\left(\frac{\dot{\gamma}t_0}{\epsilon_0}\right) + \frac{1}{\chi}\right). \tag{C1}$$

This expression is only approximate, as it neglects the term that introduces the yield stress. Using the approximate steady-state solution to the effective temperature, we can obtain an approximate solution for the steady-state flow stress as a function of temperature. By inserting the approximate solution for the steady-state effective temperature (Eq. (B3)) into the equation for the steady-state stress (Eq. (C1)), we obtain an approximate steady-state stress:

$$\sigma = \begin{cases} \frac{Q^*}{V^*} + \frac{kT}{V^*}\left(\log\left(\frac{\dot{\gamma}t_0}{\epsilon_0}\right) + \frac{1}{\hat{\chi}}\right) & T < T_c \\ \frac{Q^* - Q/\beta}{V^*} + \frac{kT}{V^*}\left(\log\left(\frac{\dot{\gamma}t_0}{\epsilon_0}\right) + \frac{1}{\hat{\chi}} + \frac{Q}{k\beta T_c}\right) & T \geq T_c \end{cases}. \tag{C2}$$

The crossover temperature is the same one as defined in Eq. (B5). This confirms that we expect to see two regimes in the flow stress data: at low temperatures, the steady-state flow stress is linearly dependent on temperature, and at higher temperatures above T_c the dependence is also linear, but with a different slope. The linear dependence of flow stress on temperature arises because of thermal activation of STZ rearrangements. The slope changes between the low-temperature regime and the high-temperature regime, because at high temperatures relaxation decreases the steady-state effective temperature and mitigates the effect of thermal activation.

In the high-temperature regime of the bulk metallic glass experiments, the data show that the flow stress exhibits a weak linear dependence on temperature. This puts a constraint on the value of the kinetically ideal effective temperature through the dependence of the flow stress on temperature. The other parameters in the approximate steady-state flow stress are easy to estimate based on the experiments, so this result provides a simple method for determining the kinetically ideal effective temperature $\hat{\chi}$. The value of the effective temperature that arises from this constraint is generally consistent with other studies using STZ Theory [56].

The solution for the steady-state effective temperature determined here is only an approximation of the actual steady-state values. In practice, the transition from a temperature-independent effective temperature at low temperatures to a temperature-dependent one at high temperatures occurs more gradually than we assume here. Therefore these calculations are useful for determining parameter values and limiting behaviors, while we employ the numerical solutions of the steady-state effective temperature to make comparisons with the experimental data in the main text.

Appendix D: Transition from Non-Serrated to Serrated Flow

Here, we provide the details of the calculation of the critical strain rate indicating the transition from non-serrated to serrated flow and how it varies with thermal temperature. While the result is straightforward, the resulting expressions are fairly complex and require a few simplifying approximations.

Our goal is to find an expression for the critical strain rate $\dot{\gamma}_{cr}$ as a function of temperature. The critical strain rate is the strain rate at which the steady-state flow stress is rate neutral, that is, $d\sigma/d\log\dot{\gamma} = 0$. Because the metallic glass data exhibit an Arrhenius scaling, we instead determine $d\log\dot{\gamma}_{cr}/d(1/T)$, which should be a constant activation energy divided by Boltzmann's constant. To do this, we determine the critical strain rate by first rearranging the main STZ equation (Eq. (2)):

$$\sigma = \frac{Q^*}{V^*} + \frac{kT}{V^*}\left[\log\left(\frac{\dot{\gamma}t_0}{\epsilon_0}\right) + \frac{1}{\chi}\right]. \tag{D1}$$

Note that this expression is only approximately true – here we assume that the stress is much larger than the yield stress. The effective temperature in this expression is the steady-state value at strain rate $\dot{\gamma}$, and is thus dependent on the strain rate. Differentiating with respect to the log of the strain rate gives

$$\frac{d\sigma}{d\log\dot{\gamma}} = \frac{kT}{V^*}\left(1 + \frac{d\left(1/\chi\right)}{d\log\dot{\gamma}}\right). \tag{D2}$$

Setting this equal to zero, we find that the critical strain rate must satisfy the following:

$$1 + \frac{d\left(1/\chi\right)}{d\log\dot{\gamma}} = 0. \tag{D3}$$

This condition tells us when the steady-state rate dependence is rate neutral, which defines the critical strain rate. This condition will be used below to determine how the critical strain rate varies with temperature.

To make use of this condition, we need to determine $d(1/\chi)/d\log\dot\gamma$ from the steady-state effective temperature. The steady-state effective temperature occurs when dissipation and relaxation balance and $d\chi/dt = 0$:

$$\frac{d\chi}{dt} = \frac{\dot\gamma\sigma}{c_0\sigma_y}\left(1 - \frac{\chi}{\hat\chi(\dot\gamma)}\right) - R\exp\left(-\frac{\beta}{\chi} - \frac{Q}{kT}\right) = 0. \tag{D4}$$

First, we rewrite as:

$$\log(\dot\gamma) + \log\left(\frac{\sigma\left(1 - \chi/\hat\chi\right)}{Rc_0\sigma_y}\right) = -\frac{\beta}{\chi} - \frac{Q}{kT}. \tag{D5}$$

This can be easily differentiated with respect to the log of the strain rate:

$$1 + \frac{1}{1 - \chi/\hat\chi}\left[\frac{\chi^2}{\hat\chi}\frac{d1/\chi}{d\log\dot\gamma} + \frac{\chi}{\hat\chi^2}\frac{d\hat\chi}{d\log\dot\gamma}\right] = -\beta\frac{d1/\chi}{d\log\dot\gamma}. \tag{D6}$$

Note that since $\hat\chi$ is a function of the strain rate, there is a $d\hat\chi/d\log\dot\gamma$ term. Using $\hat\chi = \chi_w/\log(q_0/(\dot\gamma t_0))$ (Eq. (4)), we find:

$$\frac{d\hat\chi}{d\log\dot\gamma} = \frac{\chi_w}{\left[\log(q_0/(\dot\gamma t_0))\right]^2} = \frac{\hat\chi^2}{\chi_w}. \tag{D7}$$

Using this expression, along with the condition defining the critical strain rate (Eq. (D3)), we find that

$$1 + \frac{1}{1 - \chi/\hat\chi_{cr}}\left[-\frac{\chi^2}{\hat\chi_{cr}} + \frac{\chi}{\chi_w}\right] = \beta. \tag{D8}$$

Because the kinetically ideal effective temperature is explicitly a function of the strain rate, we denote it as $\hat\chi_{cr}$ to emphasize that it is evaluated at the critical strain rate. Rearranging this yields

$$\left(\frac{1}{\chi^2} - \frac{1}{\hat\chi_{cr}\chi}\right)(\beta - 1) = \frac{1}{\chi_w\chi} - \frac{1}{\hat\chi_{cr}}. \tag{D9}$$

The effective temperature satisfies this condition at the critical strain rate.

To make use of this condition to determine the scaling between the critical strain rate and inverse temperature, we differentiate with respect to the inverse temperature:

$$\begin{aligned}(\beta - 1)&\left(\frac{2}{\chi}\frac{d(1/\chi)}{d(1/T)} - \frac{1}{\hat\chi_{cr}}\frac{d(1/\chi)}{d(1/T)} + \frac{1}{\chi\hat\chi^2}\frac{d\hat\chi_{cr}}{d(1/T)}\right)\\ &= \frac{1}{\chi_w}\frac{d(1/\chi)}{d(1/T)} + \frac{1}{\hat\chi_{cr}^2}\frac{d\hat\chi}{d(1/T)}.\end{aligned} \tag{D10}$$

Using the above result for $d\hat\chi/d\log\dot\gamma$ in Eq. (D7), we have $d\hat\chi_{cr}/d(1/T) = (\hat\chi_{cr}^2/\chi_w)d\log\dot\gamma_{cr}/d(1/T)$. Substituting this expression into Eq. (D10), we find that

$$\begin{aligned}(\beta - 1)&\left(\frac{2}{\chi}\frac{d(1/\chi)}{d(1/T)} - \frac{1}{\hat\chi_{cr}}\frac{d(1/\chi)}{d(1/T)} + \frac{1}{\chi\chi_w}\frac{d\log\dot\gamma_{cr}}{d(1/T)}\right)\\ &= \frac{1}{\chi_w}\frac{d(1/\chi)}{d(1/T)} + \frac{1}{\chi_w}\frac{d\log\dot\gamma_{cr}}{d(1/T)}.\end{aligned} \tag{D11}$$

Collecting terms on either side and dividing through by χ, we find that

$$\begin{aligned}\frac{d\log\dot{\gamma}_{cr}}{d(1/T)}&\left((\beta-1)\frac{1}{\chi\chi_w}-\frac{1}{\chi_w}\right)\\&=\left((\beta-1)\left(-\frac{2}{\chi}+\frac{1}{\hat{\chi}_{cr}}\right)+\frac{1}{\chi_w}\right)\frac{d(1/\chi)}{d(1/T)}.\end{aligned}\tag{D12}$$

Solving for $d\log(\dot{\gamma}_{cr})/d(1/T)$, we have

$$\begin{aligned}\frac{d\log\dot{\gamma}_{cr}}{d(1/T)}&=\frac{(\beta-1)\,\chi_w\left(-\frac{2}{\chi}+\frac{1}{\hat{\chi}_{cr}}\right)+1}{(\beta-1)\,\frac{1}{\chi}-1}\frac{d(1/\chi)}{d(1/T)}\\&=A\frac{d(1/\chi)}{d(1/T)},\end{aligned}\tag{D13}$$

where A is defined as the proportionality factor between $d\log\dot{\gamma}_{cr}/d(1/T)$ and $d(1/\chi)/d(1/T)$. This relates the change in the critical strain rate with temperature to the change in the effective temperature with temperature. Note that this expression depends on the effective temperature at which the transition occurs, which we can estimate using the crossover effective temperature $\chi_c=\beta((1+4\hat{\chi}/\beta)^{1/2}-1)/2$ defined in Appendix B.

Because the strain rate and the effective temperature must also satisfy the steady-state equation for the effective temperature (Eq. (D5)), we can differentiate that equation with respect to the inverse temperature to eliminate $d(1/\chi)/d(1/T)$ to obtain an expression for $d\log\dot{\gamma}_{cr}/d(1/T)$:

$$\frac{d\log\dot{\gamma}_{cr}}{d(1/T)}=-\beta\frac{d(1/\chi)}{d(1/T)}-\frac{Q}{k}.\tag{D14}$$

Here, we assume that we can neglect the temperature dependence of the $\log(1-\chi/\hat{\chi})$ term, which is a reasonable approximation in practice (note that this assumption was also made in obtaining the approximate solution to the steady-state effective temperature). Solving this simultaneously with Eq. (D13) to eliminate $d(1/\chi)/d(1/T)$, we find

$$\frac{d\log\dot{\gamma}_{cr}}{d(1/T)}=-\frac{Q}{k\left(1+\frac{\beta}{A}\right)}.\tag{D15}$$

This expression demonstrates that the critical strain rate is expected to follow an Arrhenius scaling as a function of temperature: $d\log\dot{\gamma}_{cr}/d(1/T)$ is approximately constant, and this energy scale is proportional to the activation energy for relaxation but is also dependent on the energy scale for the kinetically ideal effective temperature χ_w and the energy scale for formation of relaxation events β. For typical parameters used to match the bulk metallic glass data, $A\approx-1.33$ (this estimate varies slightly depending on the value of the strain rate at which $\hat{\chi}$ and χ_c are calculated; the results here use the values at a strain rate of 10^{-3} s^{-1}), which leads to $d \log \dot{\gamma}_{cr}/d(1/T) \approx -3Q/k = 0.48$ eV$/k$. This value is in good agreement with the value determined from the numerical solution of 0.42 eV presented in the main text.

ACKNOWLEDGMENTS

Support by the Swiss National Science Foundation (SNF Grant Nos. 200020-135100 and 200020-153103), DOE grant DE-AC52-06NA25396, and institutional (LDRD) funding at Los Alamos are gratefully acknowledged. The authors also thank R. Maaß for providing experimental data shown in Figs. 3 and 4.

---

[1] J. Lauridsen, M. Twardos, and M. Dennin, Phys. Rev. Lett. **89**, 098303 (2002).

[2] C. Marone, Annual Review of Earth and Planetary Sciences **26**, 643 (1998).

[3] H. Yoshizawa and J. N. Israelachvili, J. Phys. Chem. **97**, 11300 (1993).

[4] C. Drummond and J. Israelachvili, Phys. Rev. E **63**, 041506 (2001).

[5] M. F. Ashby and A. L. Greer, Scripta Mater. **54(3)**, 321 (2006).

[6] M. Telford, Materials Today **7(3)**, 36 (2004).

[7] J. F. Löffler, Intermetallics **11(6)**, 529 (2003).

[8] A. L. Greer, Science **267**, 1947 (1995).

[9] W. L. Johnson, MRS Bull. **24(10)**, 42 (1999).

[10] A. Inoue, Acta Mater. **48**, 279 (2000).

[11] C. A. Schuh and A. C. Lund, Nature Mater. **2(7)**, 449 (2003).

[12] J. Lu, G. Ravichandran, and W. L. Johnson, Acta Mater. **51**, 3429 (2003).

[13] A. Dubach, F. H. Dalla Torre, and J. F. Löffler, Phil. Mag. Lett. **87**, 695 (2007).

[14] C. A. Schuh, T. C. Hufnagel, and U. Ramamurty, Acta Materialia **55**, 4067 (2007).

[15] A. Greer, Y. Cheng, and E. Ma, Materials Science and Engineering: R: Reports **74**, 71 (2013).

[16] M. L. Falk and J. S. Langer, Phys. Rev. E **57**, 7192 (1998).

[17] Y. Shi, M. B. Katz, H. Li, and M. L. Falk, Phys. Rev. Lett. **98**, 185505 (2007).

[18] J. H. Dieterich, J. Geophys. Res. **84**, 2161 (1979).

[19] A. L. Ruina, Ph.D. thesis, Brown University, Providence, RI (1980).

[20] W. Götze and L. Sjögren, Rep. Prog. Phys. **55**, 241 (1992).

[21] J. M. Brader, T. Voigtmann, M. Fuchs, R. G. Larson, and M. Cates, Proc. Natl. Acad. Sci. USA **106**, 15186 (2009).

[22] D. Turnbull and M. H. Cohen, J. Chem. Phys. **52**, 3038 (1970).

[23] F. Spaepen, Acta Metall. **25(4)**, 407 (1977).

[24] A. S. Argon, Acta Metall. **27**, 47 (1979).

[25] M. L. Falk and J. S. Langer, MRS Bull. **25**, 40 (2000).

[26] J. S. Langer, Phys. Rev. E **77**, 021502 (2008).

[27] L. Li, E. Homer, and C. Schuh, Acta Materialia **61**, 3347 (2013).

[28] J. Antonaglia, W. J. Wright, X. Gu, R. R. Byer, T. C. Hufnagel, M. LeBlanc, J. T. Uhl, and K. A. Dahmen, Phys. Rev. Lett. **112**, 155501 (2014).

[29] G. Lois, A. Lemaitre, and J. M. Carlson, Phys. Rev. E **72**, 051303 (2005).

[30] E. G. Daub, M. L. Manning, and J. M. Carlson, Geophys. Res. Lett. **35**, L12310 (2008).

[31] E. G. Daub and J. M. Carlson, J. Geophys. Res. **113**, B12309 (2008).

[32] E. G. Daub, M. L. Manning, and J. M. Carlson, J. Geophys. Res. **115**, B05311 (2010).

[33] E. G. Daub and J. M. Carlson, Ann. Rev. Cond. Matt. Phys. **1**, 397 (2010).

[34] D. Klaumünzer, R. Maaß, F. H. Dalla Torre, and J. F. Löffler, Appl. Phys. Lett. **96**, 061901 (2010).

[35] D. Klaumünzer, R. Maaß, and J. F. Löffler, J. Mater. Res. **26**, 1453 (2011).

[36] R. Maaß, D. Klaumünzer, E. I. Preiss, P. M. Derlet, and J. F. Löffler, Scripta Mater. **66(5)**, 231 (2011).

[37] D. Klaumünzer, A. Lazarev, R. Maaß, F. H. Dalla Torre, A. Vinogradov, and J. F. Löffler, Phys. Rev. Lett. **107**, 185502 (2011).

[38] R. Maaß, D. Klaumünzer, G. Villard, P. M. Derlet, and J. F. Löffler, Applied Physics Letters **100**, 071904 (2012).

[39] Y. Q. Cheng, Z. Han, Y. Li, and E. Ma, Phys Rev B **80**, 134115 (2009).

[40] G. Wang, K. C. Chan, L. Xia, P. Yu, J. Shen, and W. H. Wang, Acta Materialia **57**, 6146 (2009).

[41] B. A. Sun, H. B. Yu, W. Jiao, H. Y. Bai, D. Q. Zhao, and W. H. Wang, Phys. Rev. Lett.

105, 035501 (2010).

[42] F. H. Dalla Torre, D. Klaumünzer, R. Maaß, and J. F. Löffler, Acta Materialia **58**, 3742 (2010).

[43] A. Dubach, F. H. Dalla Torre, and J. F. Löffler, Acta Materialia **57**, 881 (2009).

[44] J. R. Rice and A. L. Ruina, J. Appl. Mech. **50**, 343 (1983).

[45] A. Lemaitre and J. M. Carlson, Phys. Rev. E **69**, 061611 (2004).

[46] E. G. Daub and J. M. Carlson, Phys. Rev. E **80(6)**, 066113 (2009).

[47] D. Klaumünzer, Ph.D. thesis, ETH Zurich, Zurich, Switzerland (2012).

[48] E. D. Tabachnikova, A. V. Podolskiy, V. Z. Bengus, S. N. Smirnov, K. Y. Chernokhvostenko, A. Yavari, D. V. Luzgin, and A. Inoue, J. Alloy. Compd. **495(2)**, 345 (2010).

[49] A. Kawashima, Y. Zeng, M. Fukuhara, H. Kurishita, N. Nishiyama, H. Miki, and A. Inoue, Mater. Sci. Eng. **528(29-30)**, 8750 (2011).

[50] M. L. Falk and J. S. Langer, Annu. Rev. Condens. Matter Phys. **2**, 353 (2011).

[51] F. H. Dalla Torre, A. Dubach, J. Schällibaum, and J. F. Löffler, Acta Materialia **56**, 4635 (2008).

[52] I. K. Ono, C. S. O'Hern, D. J. Durian, S. A. Langer, A. J. Liu, and S. R. Nagel, Phys. Rev. Lett. **89**, 095703 (2002).

[53] H. J. Eyring, J. Chem. Phys. **4**, 283 (1936).

[54] M. L. Manning, E. G. Daub, J. S. Langer, and J. M. Carlson, Phys. Rev. E **79**, 016110 (2009).

[55] A. Lemaitre, Phys. Rev. Lett. **89**, 195503 (2002).

[56] J. S. Langer and M. L. Manning, Phys. Rev. E **76**, 056107 (2007).

[57] T. K. Haxton and A. J. Liu, Phys. Rev. Lett. **99**, 195701 (2007).

[58] J. Rottler and P. Maass, Phys. Rev. E **78**, 056109 (2008).

[59] W. L. Johnson and K. Samwer, Phys. Rev. Lett. **95**, 195501 (2005).

[60] S. G. Mayr, Phys. Rev. Lett. **97(19)**, 195501 (2006).

[61] D. Rodney and C. Schuh, Phys. Rev. Lett. **102(23)**, 235503 (2009).

[62] M. L. Manning, J. S. Langer, and J. M. Carlson, Phys. Rev. E **76**, 056106 (2007).

[63] B. A. Sun, S. Pauly, J. Hu, W. H. Wang, U. Kühn, and J. Eckert, Phys. Rev. Lett. **110**, 225501 (2013).

[64] E. Bouchbinder and J. S. Langer, Phys. Rev. Lett. **106**, 148301 (2011).

[65] E. Bouchbinder and J. S. Langer, Phys. Rev. E **83**, 061503 (2011).